Materials and Design 188 (2020) 108425

Contents lists available at ScienceDirect

Materials and Design

journal homepage: www.elsevier.com/locate/matdes

Evolution of the mechanical properties of a cobalt-based alloy under thermal shocks

Junxia Wen [a,b,d], Hongyan Che [c], Rui Cao [a,*], Hao Dong [c], Youxiong Ye [b], Haiyan Zhang [a], Jamieson Brechtl [e], Yanfei Gao [b,**], Peter K. Liaw [b,**]

[a] State Key Laboratory of Advanced Processing and Recycling of Non-ferrous Metal, Lanzhou University of Technology, Lanzhou 730050, China
[b] Department of Materials Science and Engineering, The University of Tennessee, Knoxville, TN 37996, USA
[c] Advanced Technology & Materials Limited Company, China Iron & Steel Research Institute Group, Beijing 100081, China
[d] School of Mechanical and Electrical Engineering, Liuzhou Vocational &Technical College, Liuzhou 545006, China
[e] The Bredesen Center for Interdisciplinary Research and Education, The University of Tennessee, Knoxville, TN 37996, USA

HIGHLIGHTS

- Mechanical properties evolution under thermal shocks was evaluated by nano-indentation tests.
- Discussed the relations of the residual stress and dislocations with the nanoindentation results
- Residual stress was calculated by the Suresh model.
- The carbide particles and precipitates are the most probable locations where the cracks initiate.

GRAPHICAL ABSTRACT

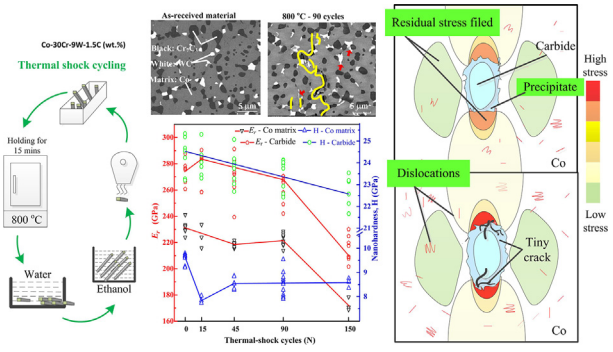

ARTICLE INFO

Article history:
Received 8 October 2019
Received in revised form 8 December 2019
Accepted 12 December 2019
Available online 13 December 2019

Keywords:
Cobalt-based alloy
Thermal shocks
Nanoindentation test

ABSTRACT

A cobalt-base alloy manufactured by hot isostatic pressing sintering (HIP) was investigated in the present work. A series of quenching thermal-shock experiments were carried out to study the effects of thermal-cycle shocks on this new cobalt-based alloy. Scanning Electron Microscope (SEM) and Energy Dispersion Spectrum (EDS) were employed to observe the evolution of microstructures under thermal-shock cycles. Results show that some floccus Co_3W_3C precipitated around the WC particles after several thermal-shock cycles. These precipitates and the carbide particles correspond to the locations with the high-stress concentration. The mechanical properties evolution under thermal-shock cycles was analyzed by Nanoindentation tests. The nanohardness presents no noticeable change with thermal-shock cycles. However, the reduced modulus demonstrates a decreasing trend with the thermal-shock cycles. The variation of the mechanical properties has an unestimated relationship with the residual stress and densities of dislocations caused by thermal shocks. Furthermore, the present work pointed out that the precipitates around the carbides are the places where the thermal fatigue crack initiated. How to deal with the precipitates will be the optimized way for this material.

* Corresponding author.
** Corresponding authors at: Department of Materials Science and Engineering, The University of Tennessee, Knoxville, TN 37996, USA.
E-mail addresses: caorui@lut.cn (R. Cao), ygao7@utk.edu (Y. Gao), pliaw@utk.edu (P.K. Liaw).

https://doi.org/10.1016/j.matdes.2019.108425

1. Introduction

The cobalt-based alloy has a typical heterogeneous microstructure of a ductile cobalt matrix and refractory carbide particles, resulting in superior high-temperature mechanical performance [1]. Furthermore, the cobalt-based alloy has excellent resistance of high temperature and high hardness when alloyed with cemented carbides. This alloy is widely used in material machining, mining machinery, aerospace, and nuclear industry, which requires great hardness, high wear resistance, and elevated-temperature resistance [2–6]. Thermal-fatigue cracking, which is attributed to its working condition, is one of the main life-limiting factors for the cobalt-based alloy [7]. This phenomenon is typically associated with cycles of heating and cooling.

The thermal-shock cycle, which is similar to the thermal-shock fatigue behavior, is characterized by the rapid cycling of the temperatures. During this process, the tremendous thermal stress is generated [8,9] in the specimens since the rate of change in the temperatures far exceeds that of the rate of the volume expansion. Consequently, significant damage and failure will occur in the specimen after the number of thermal-shock cycles reaches a threshold value [10].

Two types of strengthening mechanisms are commonly in the cobalt-based alloy strengthening. The first one is solution strengthening by adding refractory elements, such as Mo and W solutes, to the Co matrix. The second is precipitation strengthening by precipitating or adding some of W- or Cr- carbides, e.g., MC, M_3C_2, $M_{23}C_6$, M_7C_3, and so on [11,12].

Failure caused by cyclic loading or heating cycles during the application of the cobalt-based alloy has become an important aspect in recent years. Kübarsepp, Klaasen et al. [13–15] focused on the abrasive properties of carbide cements under wear conditions. They found that the WC-based cermets (cemented with Co) have an advantage over other TiC-carbide-based composites in terms of their abrasive and erosive behavior [15]. However, during cyclic-loading conditions, as compared to the TiC-based cermets in the metal forming performance, the WC-based cermets have lower performance, which arises from the low adhesive wear resistance and higher fatigue sensitivity [15]. Biro [16–18] studied the cracks and the oxidation behavior of the Stellite 6 coating during the thermal-fatigue test. Tang et al. [19] investigated the thermo-mechanical fatigue (TMF) of the wrought Co–Cr–Mo alloy. The conditions of the TMF test consisted of an out-of-phase program to simulate the service condition. The out-of-phase program refers to that the phase difference between the waves of temperature and mechanical strain is 90°. The $\gamma \rightarrow \varepsilon$ martensitic transformation was observed and thought to be responsible for the hardening effect of the Co–Cr–Mo alloy during the TMF test. Tunthawiroon et al. [20] investigated the isothermal fatigue (IF) behavior of a single ε-phase of Co–Cr–Mo alloys at different temperatures and under various applied strain-controlled processes. At 700 °C, oxidation-fatigue interactions are the main failure modes in the Co–Cr–Mo alloy.

Series studies indicated that both higher temperatures and larger applied strain amplitudes could result in shorter fatigue lives. Wu, et al. [7] performed a series of quenching thermal-fatigue tests and detected the microstructural evolution and crack propagation in laser-deposited Stellite 6 alloys by various methods. They found that thermal cracks always propagate along with the net-like eutectic structures and γ/ε interfaces. Based on these studies, it can be concluded that oxidation and strain-induced or temperature-induced martensitic transformation play an important role in the failure of the Co-based alloy under thermal fatigue. What is more, carbides are sensitive to fatigue and oxidation. All of these factors are intrinsic properties of cobalt-base alloys. How to find out the main factor and find the optimization under the assigned condition is becoming an important issue.

In the present work, a series of quenching thermal-shock experiments were conducted firstly. Then the residual mechanical parameters of the specimens were characterized by the nanoindentation experiments to investigate the effects of thermal shocks on this cobalt-based alloy.

2. Experimental methods

2.1. Material and specimens

The hot-isostatic-pressing process (HIP) was used to manufacture this new cobalt-based alloy. The main composition is Co-30Cr-9W-1.5C (weight percent, wt%). The diameters of the original powder supplied are ranged from 2 to 20 μm.

Specimens were machined by electric-spark machining (ESM). The specimen dimensions are $3 \times 4 \times 36$ (mm), and $0.1 \times 45°$ chamfers were manufactured on the four long edges. All of the surfaces were polished to ensure the uniform stress distribution on the edges and surfaces during testing. The polishing work was ground on the silicon carbide grinding paper gradually from 120-grit to 600-grit.

The nanoindentation experiments were carried out on mirror qualified surfaces. The tested surfaces were firstly mechanically grounded by 240 grit, 400 grit, 800 grit, and 1200 grit silicon carbide papers sequentially and then were additionally vibration-polished for 24 h using a 0.05 μm colloidal SiO_2 suspension.

The microstructures before and after the thermal-shock tests were investigated by scanning electron microscope (SEM, JSM-7001F/JEOL). Phase identifications of the specimens before and after the thermal-shock tests were analyzed by the X-ray diffraction (XRD) technique using an X' Pert PRO X-ray diffractometer with a Cu-Kα1 radiation source.

2.2. Thermal-shock test

The thermal-shock procedure is shown in Fig. 1. One group of specimens was put into the furnace which has already been 800 °C. After 15 min holding at 800 °C, the specimens were put into water at room temperature (RT) quickly and then dried up by ethanol and air dryer. Every set of six specimens is one group that experienced the same cycles of thermal shocks at the same temperature. The experiments involved 15, 45, 90, and 150 cycles of thermal shocks.

2.3. Nanoindentation test

The Hysitron Triboindenter (Hysitron, Inc., USA) was employed to analyze the effects of thermal shocks on the mechanical properties of different phases in this new cobalt-based alloy. Nanoindentation experiments were performed on the specimens that are virgin as received and have been thermal-shocked 15, 45, 90, 150 cycles. A diamond Berkovich tip was used, and its area function was calibrated with a fused silica specimen. Nanoindentation tests were performed using a maximum load of 2000 μN with a loading rate of 400 μN/s, and a holding time of 2 s at the peak load before unloading. The unloading rate was equal to the loading rate. For each phase, at least five particles were randomly picked out to do the nanoindentation test. Scanning probe microscopy (SPM) integrated with the nanoindentation system was adopted to characterize the indentation behavior. The obtained load-depth curves were analyzed according to the Oliver & Pharr method [21,22].

3. Experimental results

3.1. Microstructures and microcracks

The microstructures of the as-received material are the Cr_7C_3, WC, and Co matrix, which appears as the black particles, white particles, and grey matrix, respectively, marked in white lines in Fig. 2(a). The microstructures after different cycles of the thermal-shock test at temperatures ranging from 800 °C to RT are presented in Fig. 2(b), (c) and (d). The red arrows correspond to the newly-formed Co_3W_3C phases around the WC particles. The yellow lines are the microcracks generated in the process of thermal shocks. Most of the microcracks are produced across

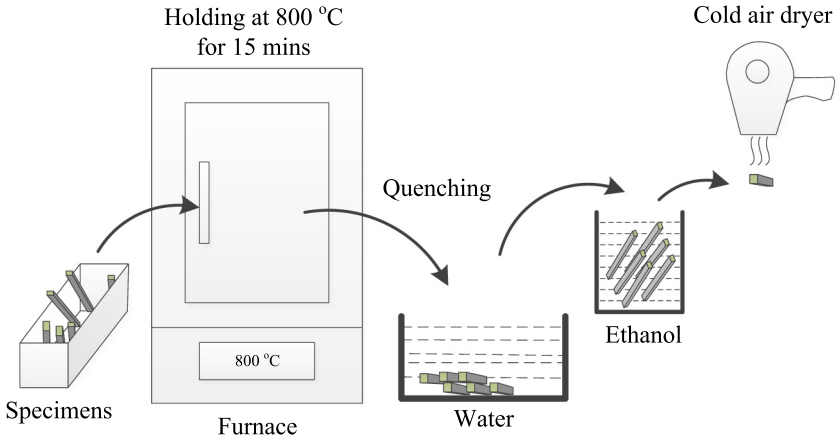

Fig. 1. Schematic illustration of one cycle of thermal shock.

or around the white WC particles and the black Cr_7C_3 particles, very a few microcracks appeared in the matrix.

3.2. XRD analysis of the phase before and after thermal shock

Fig. 3 presents the XRD analysis of the as-received cobalt-based alloy material and the specimen after 150 cycles of thermal shocks at temperatures ranging from 800 °C to RT. As identified in Fig. 3, the main phases in the cobalt-based alloy are ε-Co, Cr_7C_3, WC, $Cr_{23}C_6$, and Co_3W_3C, and there is no obvious change after 150 cycles of thermal shocks. It is because of the increased intensity of the new phases in thermal-shock cycles is comparatively too little to be detected.

The EDS line-scanning across the interfaces were conducted to reveal the effect of the thermal shocks on the microstructure of this new cobalt-based alloy. Here, the average diffusion distances for the different elements in the cobalt-based alloy before and after 150 cycles of thermal shocks were evaluated. Fig. 4(a) presents the line-scanning map of the as-received material. Fig. 4(b) displays the line-scanning map of the specimen after 150 thermal-shock cycles at temperatures ranging from 800 °C to RT. The red arrow in Fig. 4(b) presents a platform in the EDS line for the Co in the WC particle, which results from the formation of Co_3W_3C at the interface of the WC and Co matrix. Importantly, Fig. 4(c) illustrates that the elements, W and Co, have the longest inter-diffusion distance.

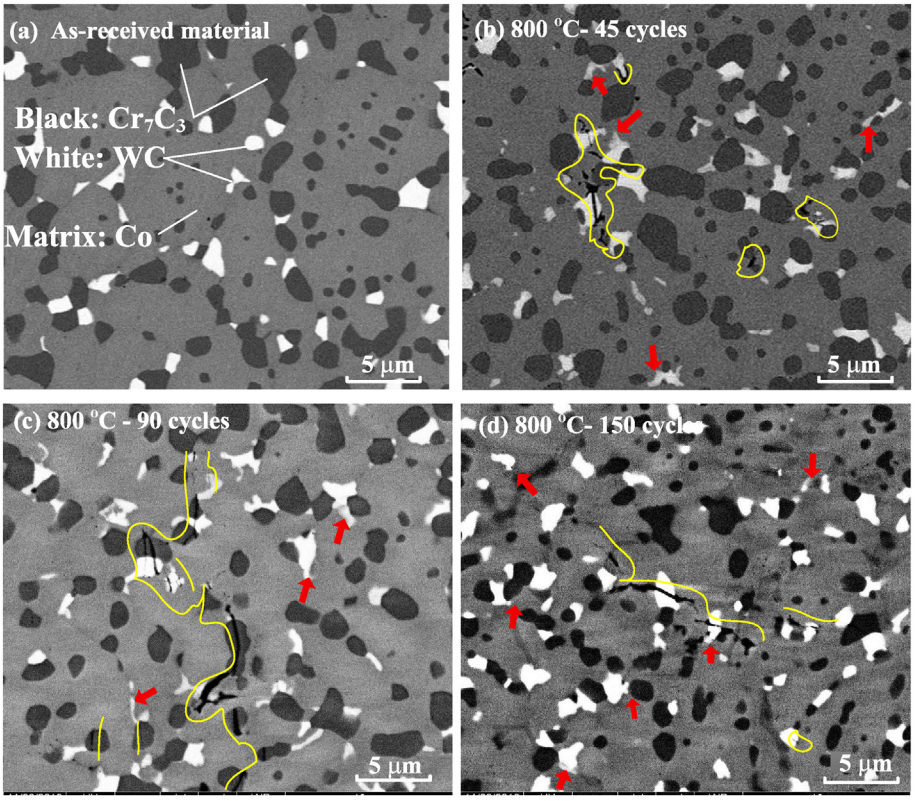

Fig. 2. The microstructures of the as-received material and microstructure and microcracks after different cycles of thermal shocks at temperatures ranging from 800 °C to RT. (a) As-received material, (b) 800 °C - 45 cycles, (c) 800 °C - 90 cycles, (d) 800 °C - 150 cycles. The red arrows correspond to the newly-formed Co_3W_3C phases around the WC particles. The yellow lines demonstrate the microcracks in the microstructure. (For interpretation of the references to colour in this figure legend, the reader is referred to the web version of this article.)

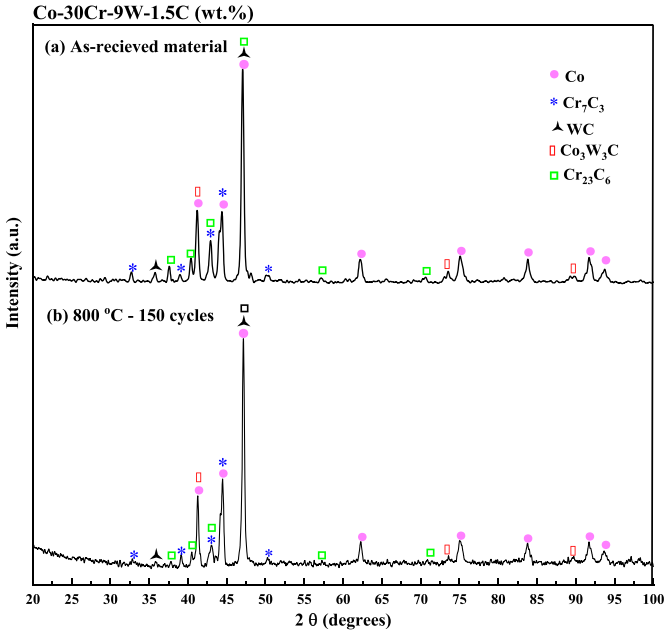

Fig. 3. XRD analysis of the as-received material and that after 150 cycles of thermal shocks at temperatures ranging from 800 °C to RT.

3.3. Evolution of mechanical properties of the Co matrix and carbides after different cycles of thermal shocks

The effects of thermal shocks on different phases in the cobalt-based alloy have been revealed by the nanoindentation test. Fig. 5 is the representative SPM image of nano-indents on the cobalt-based alloy. In this paper, indents located on phase boundaries (e.g., Indents 2 and 5 in Fig. 5) were not taken into account. The white phases and black phases are called as carbides for general because of their similar behaviors in the nanoindentation tests.

Fig. 6 shows the load-depth curves of the cobalt matrix and the carbides before and after different cycles of thermal shocks at temperatures ranging from 800 °C to RT. These curves belong to some randomly-picked indentation points included in Figs. 7 and 8. From Fig. 6(a) and (b), it can be seen that the load-depth curves of the Co matrix and the carbides shift to greater depth values after 150 cycles of thermal shocks. In general, the load-depth curves vacillate to the right with the increase cycles of thermal shocks.

Fig. 7 is the maximum displacement, h_{max}, of the Co matrix and the carbides. They are important parameters acquired from the load-depth curves and are used to calculate the residual stress [23]. h_{max} on the as-received material is marked by 0 cycle in Fig. 7. Overall, the h_{max} values of the carbide increase with the increase of thermal-shock cycles. The h_{max} values of the Co matrix show no noticeable change with the increase thermal-shock cycles after a sharp increase after 15 cycles of thermal shocks.

Fig. 8 presents the variation of the reduced modulus(E_r) and nanohardness(H), of the Co-matrix and carbides before and after different cycles of thermal shocks at temperatures ranging from 800 °C to RT. The variations of the reduced modulus of carbides have a similar trend to that of the Co matrix. The reduced modulus of the Co matrix and carbides declines markedly after 150 cycles of thermal shocks but shows no noticeable change before 90 cycles, as shown in Fig. 8(a). However, the nanohardness of the Co matrix has no noticeable change with the growth of thermal-shock cycles after 15 thermal-shock cycles, the nanohardness of the carbides shows a slightly decreasing trend with the increase of thermal shocks, as presented in Fig. 8(b).

4. Discussion

4.1. Precipitates and diffusion at the interfaces

New carbides would precipitate when WC is coated on the surface of other alloys, especially at high temperatures [24–29]. One typical precipitate in the cobalt-based alloy is M_6C [24]. Huang et al. [25] demonstrated two ways in which Fe_3W_3C precipitates in the composite material of the WC/Steel at the interface of the WC particle and the Fe matrix. The first way involves W and C atoms that have decomposed

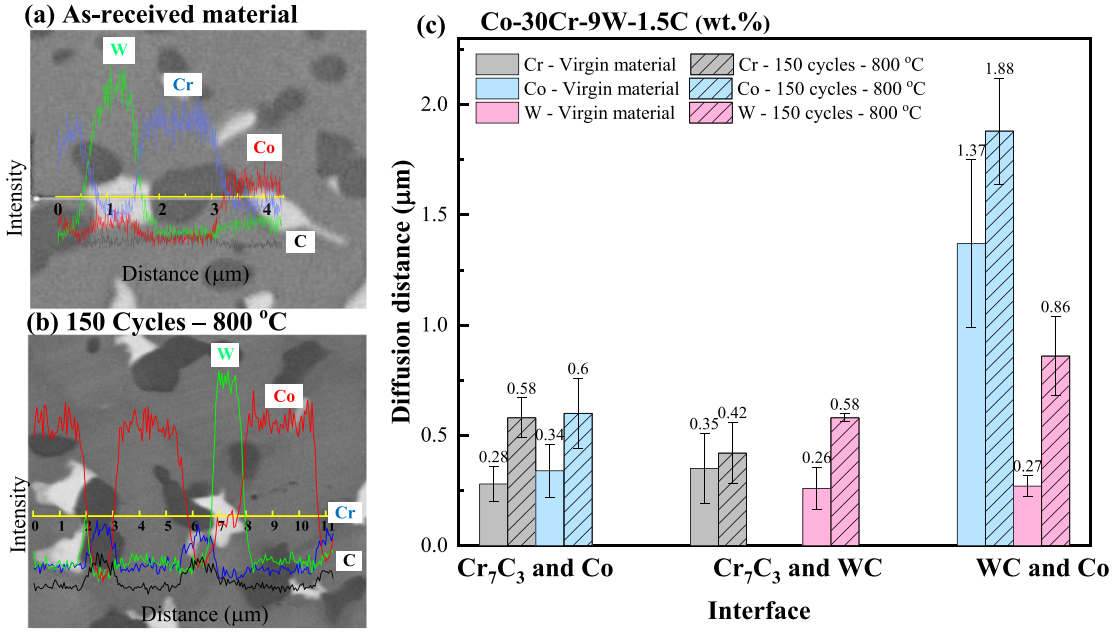

Fig. 4. EDS line scanning and the diffusion distances between different phases before and after 150 cycles of thermal shocks at temperatures ranging from 800 °C to RT. (a) EDS line scanning across the Co/WC/Cr_7C_3/Co interfaces in the as-received material, (b) EDS line scanning across different interfaces in the specimen that has been subjected to 150 cycles of thermal shocks at temperatures ranging from 800 °C to RT. The red arrow shows the platform in the Co EDS line in the WC particle. (c) Statistic of diffusion distances at interfaces before and after 150 cycles of thermal shock. (For interpretation of the references to colour in this figure legend, the reader is referred to the web version of this article.)

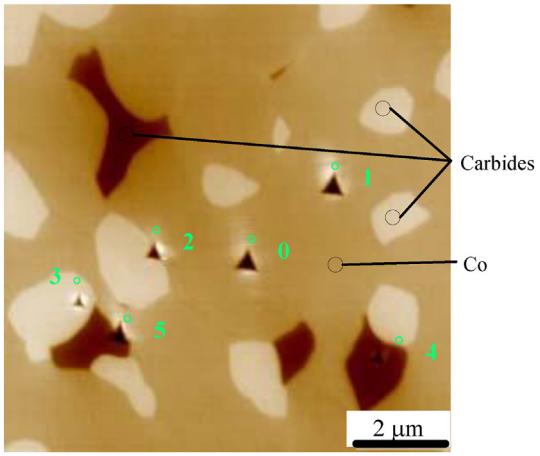

Fig. 5. Representative SPM image showing the indents on the cobalt-based alloy.

from the WC particle and subsequently combine with the highly concentrated Fe atoms to form the Fe_3W_3C phase. The second way consists of W_2C particles that are inherent in the WC particle, which reacts with the Fe that has diffused into the WC particle to form the Fe_3W_3C phase. The hard phase Fe_3W_3C is one type of M_6C. It can be inferred that there

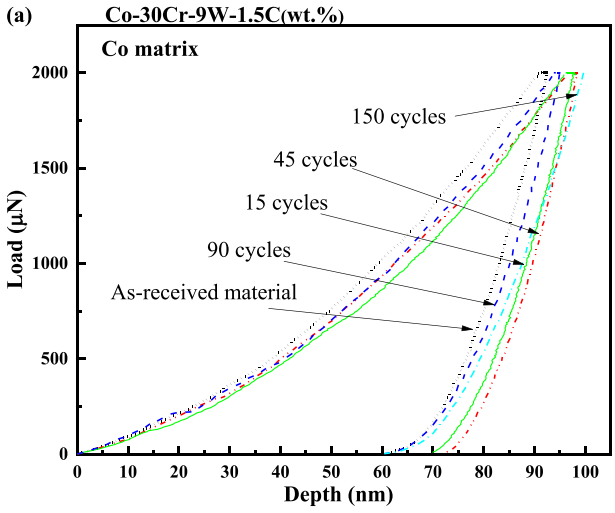

Fig. 6. Load-depth curves of the Co matrix and the carbides before and after different cycles of thermal shocks at temperatures ranging from 800 °C to RT. (a) Load - depth curves of the cobalt matrix. (b) Load - depth curves of the carbides.

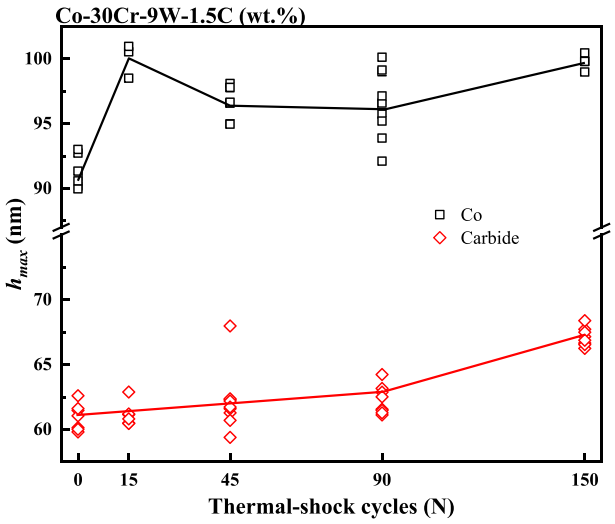

Fig. 7. h_{max} values of specimens before and after different cycles of thermal shocks at temperatures ranging from 800 °C to RT.

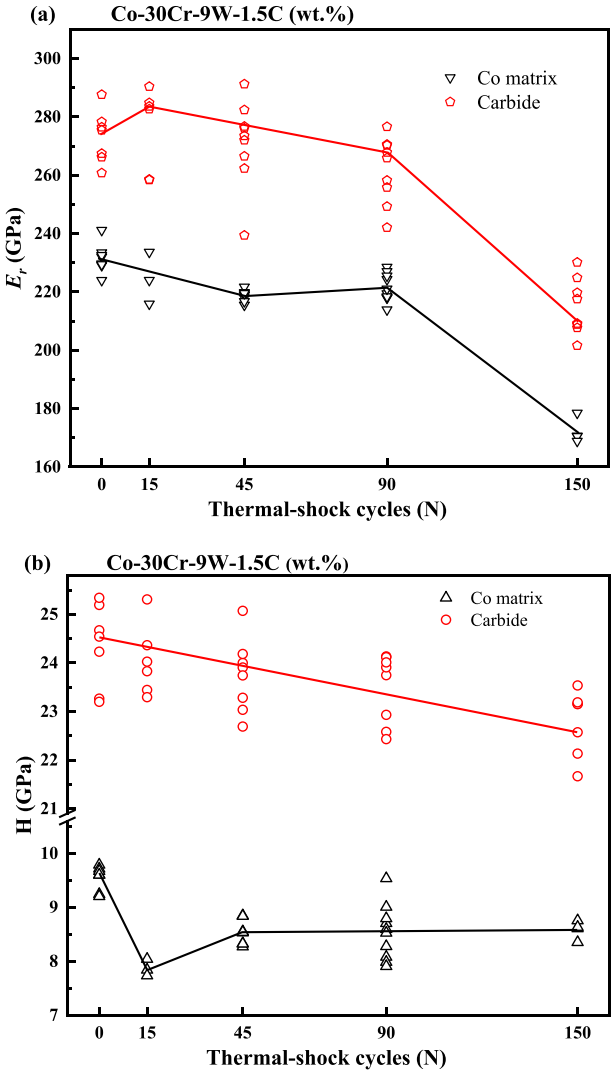

Fig. 8. Reduced modulus and nanohardness before and after different cycles of thermal shocks at temperatures ranging from 800 °C to RT. (a) Reduced modulus – thermal-shock cycles. (b) Nanohardness – thermal-shock cycles.

are two similar ways in which Co_3W_3C precipitates in the WC-Co alloy at the interface of the WC particle and Co matrix.

Based on the experimental results, the diffusion is inter-diffusion between the carbides and the matrix. According to the line scanning data presented in Fig. 2(b), and the diffusion distance increase with the increase of the thermal-shock cycles. The diffusion distance between the WC and Co matrix is longer than that between the Cr_7C_3 and Co matrix.

The cobalt-based alloy in this research consists of two kinds of carbides (WC and Cr_7C_3). The W atoms in the WC particles and Cr in the Cr_7C_3 particles will diffuse into the Co matrix, while the Co atoms would diffuse into the WC and Cr_7C_3 particles. New carbides, such as Co_nW_nC, would form at the interfaces of the WC particles and the Co matrix [30–32], which coincides with Fig. 2. Carbides, $M_{23}C_6$, would form at the interface of the Cr_7C_3 particles and the Co matrix [33].

It is reported that Co inclines to form M_6C in the cobalt-based alloy, and will form Co_3W_3C in the W-rich cobalt-based alloy [34]. In the W—C binary alloy system, WC would precipitate at the eutectic point. However, in the M(Fe, Co, Ni)-W-C ternary alloy system, it tends to form the carbide of M_6C [35] with the increased content of W. This has been evidenced by Zhong et al. [36]. They illustrated the in situ solid-phase diffusion-controlled formations of M_6C in their research work of the WC reinforced Fe-matrix surface composite. Because the formation energy of M_3Co_3C is lower than that of M_6W_6C [37], the most possible precipitation around the WC particle in this new Cobalt-based alloy is Co_3W_3C.

4.2. The evolution of E_r and H

Many factors will affect the results gained from nanoindentation tests. The first factor for the above trends in Fig. 8 is the residual stress caused by the repeated quenching process. The maximum depth, h_{max}, which is thought to be related to the residual stress [23]. Generally, the value of h_{max} will be large when there is tensile residual stress and small when there is compressive residual stress [38,39]. Similarly, some researchers insisted that the tensile residual stress diminishes hardness while trend in compressive residual stress gives rise to hardness [40–43]. However, some research [44–46], which focused on analyzing the residual stresses employing instrumental indentation techniques, suggested that applied (residual) stresses will cause a degradation of the reduced modulus, while the nanohardness is not significantly affected by applied (residual) stresses.

The residual stress in Fig. 9 is calculated by Suresh model [47]. Tensile residual stress is calculated by Eq. (1) and compressive residual stress is calculated by Eq. (2).

$$\sigma = H\left(1-\frac{h_0^2}{h^2}\right) \tag{1}$$

$$\sigma = \frac{H}{sin\alpha}\left(\frac{h_0^2}{h^2}-1\right) \tag{2}$$

where H is the nanohardness. h_0 is the maximum displacement obtained by Nanoindentation on the no residual stress specimen. However, it is too hard to obtain the no residual stress sample. Here, h_0 is calculated by the average value of h_{max} on the as-received material. α is the angle between the indenter tip and the tested surface, for Berkovich indenter, α is 24.7°.

Comparing to the as-received material, most of the calculated residual stress in the Co matrix and carbides after different thermal-shock cycles are tensile stress. The residual stresses in the carbides present a large scatter in Fig. 9. The residual stresses in the carbides show an increasing trend with the increase cycles of thermal shocks and reach the maximum value at 150 cycles of thermal shocks.

The second factor is the density of dislocations. Similar results were obtained in the research work of Damadam et al. [48]. They pointed out

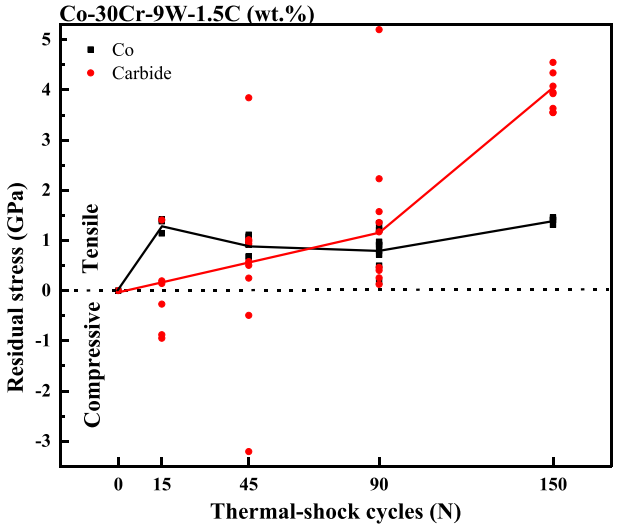

Fig. 9. Residual stress before and after different cycles of thermal shocks calculated by Suresh model [47].

that the increased density of dislocations will decrease the modulus of the tested material. The decreased modulus was also observed on the pre-existing dislocations materials in the research work of Barnoush's [49,50]. At the same time, the loading-depth curve moved left on the tested material with pre-existing dislocations, compared to the low-density dislocations material in Barnoush's work. Accordingly, the values of h_{max} decreased with the pre-existing dislocations. This feature coincides with the results in the present work.

4.3. Microcrack initiation and propagation

The B/G ratio is a criterion [51], which determines whether a given material is brittle or ductile. A higher B/G ratio indicates that a material is more ductile and vice-versa. The B/G ratios of the possible phases in this Stellite 12 alloy are shown in Table 1. As can be observed in Table 1, all of the carbides dispersed in the Co matrix have a lower B/G ratio, indicating that they are relatively less ductile (or more brittle). WC is always the most brittle phase in this cobalt-based alloy.

There are significant differences between the shear and the elastic moduli of the Co matrix and WC phase. For instance, the stiffness tensor of the WC [52] is very large, while the stiffness tensor of the Co [58] is very small. The shear strength of WC [52] is minimal, while that of Co [58] is very high. The significant difference between the WC and Co matrix will induce the initiation and propagation of cracks at their interface.

As discussed in Section 4.1, Co_3W_3C would precipitate around the WC particle due to the accelerated diffusion between the WC particles and the Co matrix. The B/G ratios of the Co_3W_3C are 2.22, and it has brittle nature. Li et al. [59] investigated the thermal-fatigue mechanism of the WC-particles reinforced composite at different thermal-shock

Table 1
The mechanical properties of materials.

Materials	Shear modulus G_{VRH} (GPa)	Bulk modulus B_{VRH} (GPa)	B/G ratio
WC [52]	231	358	1.55
fcc-Co (calculated)	182	61	3.0
Cr_7C_3 [53]	144	312	2.16
Co_3W_3C [54]	158	352	2.22
$Cr_{23}C_6$ [55]	138	291	2.11

The mechanical properties of fcc-Co were calculated following the method provided in reference [56]. The elastic constants Cij used to calculate the mechanical properties of fcc-Co were from reference [57].

temperatures. The results showed that the fatigue failure of the WC particle was influenced by thermal stress and oxidation. Under the low-temperature (500 °C), thermal stress is the major factor. However, oxidation is the primary factor at elevated temperatures (800 °C). Liu et al. [60] demonstrated the plastic deformation and crack initiation in the WC particle under the high-stress state. The various inhibitors, such as VC, Cr_3C_2, TiC, TaC, and NbC, inhibit the WC grain growth effectively. Wu et al. [7] conducted a quenching thermal-fatigue test on a laser-deposited Stellite 6 coated alloy to reveal the mechanism of the microstructural evolution and crack propagation in the coated layer. The results showed that the newly- formed γ/ε interfaces acted as paths for thermal-crack propagation because the γ → ε martensitic transformation had been activated due to fast cooling rate and thermal stress. A stress concentration is generated via the tip effect induced by the irregular shape of WC, which will be accelerated with the increasing number of thermal-shock cycles [61]. Hence, the interface between the WC and Co matrix is a location with the high-stress concentration and might be susceptible to the thermal-crack initiation.

Fig. 10 displays a schematic map of the microcrack initiation and propagation during the thermal-shock process. After several thermal-shock cycles, there is a little residual tensile stress generated in the Co matrix, Fig. 10(a). The thermal stress caused by the sharp temperature variation will accumulate at sharp corners around the carbide particles with increasing the number of thermal-shock cycles. As the number of cycles increases, the residual stress around the carbide particles will continually increase. At the same time, carbide particles will impede the propagation of stress and induce dislocations, resulting in piling up of dislocations around the carbide particles, Fig. 10(b).

The diffusion distance increases with the increase of thermal-shock cycles, and stress concentration will be aggravated by this newly-formed precipitates at the interface of the carbide particles and Co matrix, especially at the interface of the WC and Co matrix. The precipitates compound has a low shear strength, leading to a decrease of the reduced modulus and acting as the stress-concentration sits. The aggravation effect will be worse when the precipitate appears in the shape of thin films at the interfaces. The interface of the carbide particles and the Co matrix, as shown in Fig. 10(c), will be a primary contributing factor for the initiation of microcracks. As the number of thermal-shock cycles increases, these microcracks will grow into through-wall cracks, as exhibited in Fig. 10(d).

5. Conclusion

In this paper, the mechanical properties evolution of one cobalt-based alloy under thermal shocks was investigated by Nanoindentation tests.

1. Results from the nanoindentation tests show that the reduced modulus decreases significantly after 150 cycles of thermal shocks at temperatures ranging from 800 °C to RT.
2. This mechanical properties evolution was affected by the residual stress and the density of dislocations caused by thermal shocks.
3. Regions close and adjacent to the carbide particles are the most probable location that cracks initiate.

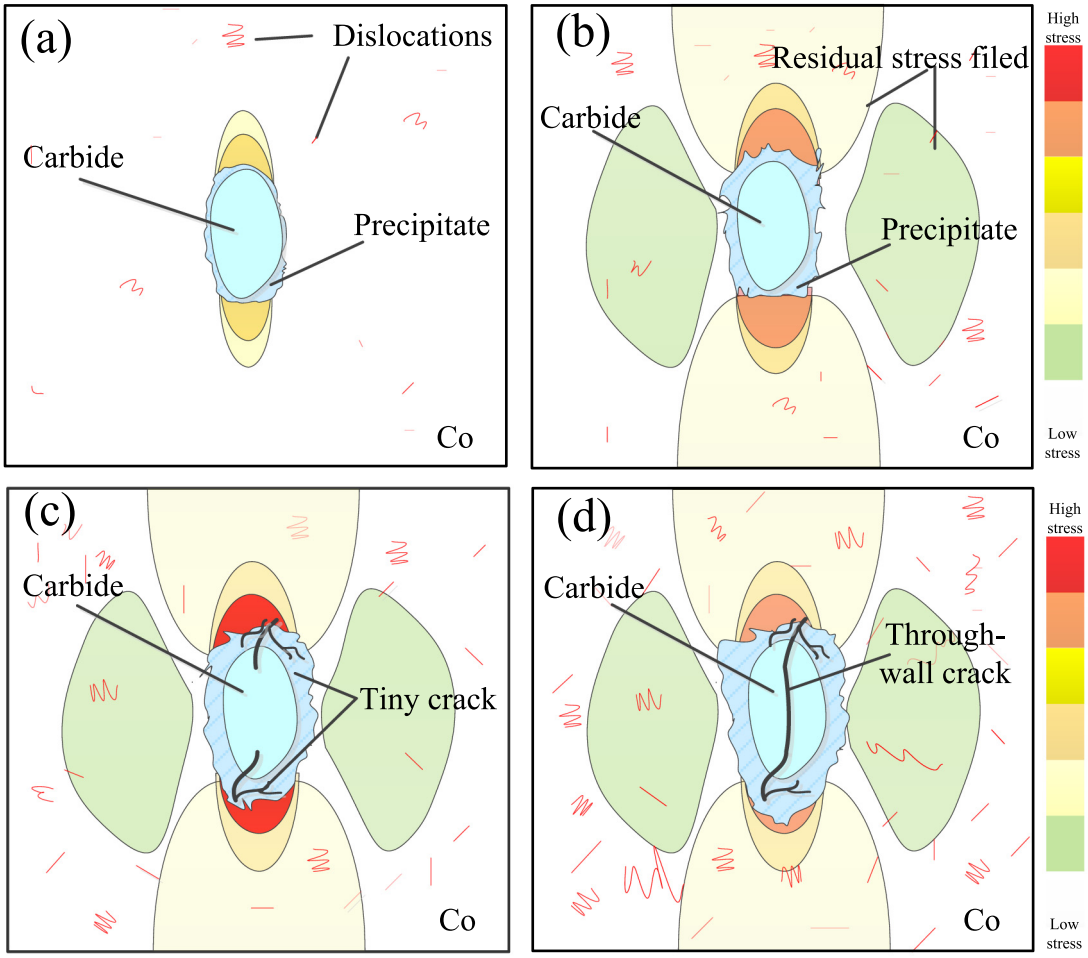

Fig. 10. Crack initiation and propagating during the thermal-shock process. (a) Dislocations decrease at the initial stage of thermal fatigue. (b) Dislocations pile-up and stress concentration at the tips of the carbide particle. (c) Crack initiation at the interface of carbide/Co. (d) Through-wall crack in the carbide particle.

CRediT authorship contribution statement

Junxia Wen: Data curation, Investigation, Methodology, Visualization, Writing - original draft, Writing - review & editing. **Hongyan Che:** Resources. **Rui Cao:** Conceptualization, Funding acquisition, Investigation, Methodology, Writing - review & editing. **Hao Dong:** Resources. **Youxiong Ye:** Data curation. **Haiyan Zhang:** Data curation. **Jamieson Brechtl:** Writing - review & editing.**Yanfei Gao:** Conceptualization, Funding acquisition, Investigation, Methodology, Writing - review & editing.**Peter K. Liaw:** Conceptualization, Funding acquisition, Investigation, Methodology, Writing - review & editing.

Declaration of competing interest

The authors declare that they have no known competing financial interests or personal relationships that could have appeared to influence the work reported in this paper.

Acknowledgments

This investigation was supported by the National Natural Science Foundation of China (Nos. 51761027, 51675255). J.X. Wen very much thanks to the support from the excellent students studying abroad foundation of Lanzhou University of Technology. We would also like to thank Dr. T. Dai for his comments. Y.X. Ye would also like to acknowledge funding from the State of Tennessee and Tennessee Higher Education Commission (THEC) through their support of the Center for Materials Processing (CMP). PKL very much appreciates the support of the National Science Foundation (DMR-1611180 and 1809640) with the program directors, Drs. G. Shiflet and D. Farkas.

References

[1] R. Cao, H. Zhang, G. Liu, H. Che, J. Chen, Effect of thermal cycle shocking on microstructure and mechanical properties of Stellite 12 (Co-29Cr-2.3 C-3W) cobalt based alloy, Mater. Sci. Eng. A 714 (2018) 68–74.
[2] M. Chandrashekar, K.V. Sreenivasa Prasad, The effect of cobalt on wear behavior of cemented carbide cutting tools for machining of titanium alloy, Materials Today: Proceedings 5 (2018) 7678–7684.
[3] S.D. Sakuntala Nahak, S. Chattopadhyaya, S. Hloch, Characterization of failure behavior in distorted WC-co tip of coal mining picks, J. Fail. Anal. Prev. 17 (1) (2017) 136–143.
[4] S. Fathi, S. Zangeneh, M. Pahlavani, A comprehensive analysis of premature failure in a cobalt-based superalloy X-45 gas turbine vane, J. Fail. Anal. Prev. 19 (5) (2019) 1337–1347.
[5] M. Kamiński, P. Budzyński, Tribological properties of Stellite 6 cobalt alloy implanted with nitrogen ions determined in the tests conducted in engine fuel atmosphere, Advances in Science and Technology Research Journal 11 (4) (2017) 215–219.
[6] A. Motallebzadeh, S.A.A. Dilawary, E. Atar, H. Cimenoglu, High-temperature oxidation of Stellite 12 hardfacings: effect of Mo on characteristics of oxide scale, J. Mater. Eng. Perform. 28 (2018) 463–474.
[7] Y. Wu, Y. Liu, H. Chen, Y. Chen, H. Li, W. Yi, Microstructure evolution and crack propagation feature in thermal fatigue of laser-deposited Stellite 6 coating for brake discs, Surf. Coat. Technol. 358 (2019) 98–107.
[8] P. Dufrénoy, G. Bodovillé, G. Degallaix, Damage mechanisms and thermomechanical loading of brake discs, European Structural Integrity Society 29 (2002) 167–176.
[9] P. Dufrénoy, D. Weichert, A thermomechanical model for the analysis of disc brake fracture mechanisms, J. Therm. Stresses 26 (2003) 815–828.
[10] H. Samrout, R.E. Abdi, Fatigue behaviour of 28CrMoV5-08 steel under thermomechanical loading, Int. J. Fatigue 20 (1998) 555–563.
[11] Q.Y. Hou, J.S. Gao, F. Zhou, Microstructure and wear characteristics of cobalt-based alloy deposited by plasma transferred arc weld surfacing, Surface & Coatings Technology 194 (2005) 238–243.
[12] C. Lee, H. Park, J. Yoo, C. Lee, W.C. Woo, S. Park, Residual stress and crack initiation in laser clad composite layer with Co-based alloy and WC + NiCr, Appl. Surf. Sci. 345 (2015) 286–294.
[13] H. Klaasen, J. Kübarsepp, A. Tšinjan, F. Sergejev, Performance of carbide composites in cyclic loading wear conditions, Wear 271 (2011) 837–841.
[14] H. Klaasen, J. Kübarsepp, I. Preis, Wear behaviour, durability, and cyclic strength of TiC base cermets, Mater. Sci. Technol. 20 (2004) 1006–1010.
[15] H. Klaasen, J. Kübarsepp, Abrasive wear performance of carbide composites, Wear 261 (2006) 520–526.
[16] Y. Birol, Thermal fatigue testing of Stellite 6-coated hot work tool steel, Mater. Sci. Eng. A 527 (2010) 6091–6097.
[17] Y. Birol, Thermal fatigue testing of Inconel 617 and Stellite 6 alloys as potential tooling materials for thixoforming of steels, Mater. Sci. Eng. A 527 (2010) 1938–1945.
[18] Y. Birol, A novel C-free Co-based alloy for high temperature tooling applications, Mater. Sci. Eng. A 528 (2011) 1117–1124.
[19] N. Tang, Y. Li, P. Tunthawiroon, Y. Koizumi, A. Chiba, Thermo-mechanical fatigue test of a wrought Co-based alloy as potential tooling material for die casting, Mater. Sci. Eng. A 615 (2014) 164–168.
[20] P. Tunthawiroon, Y. Li, Y. Koizumi, A. Chiba, Strain-controlled iso-thermal fatigue behavior of Co–29Cr–6Mo used for tooling materials in Al die casting, Mater. Sci. Eng. A 703 (2017) 27–36.
[21] W. Oliver, G. Pharr, An improved technique for determining hardness and elastic modulus using load and displacement sensing indentation experiments, J. Mater. Res. 7 (1992) 1565.
[22] W.C. Oliver, G.M. Pharr, Measurement of hardness and elastic modulus by instrumented indentation: advances in understanding and refinements to methodology, J. Mater. Res. 19 (2004) 3–20.
[23] J. Jang, Estimation of residual stress by instrumented indentation: a review, J. Ceram. Process. Res. 10 (2009) 391–400.
[24] A. Antoni-Zdziobek, J.Y. Shen, M. Durand-Charre, About one stable and three metastable eutectic microconstituents in the Fe–W–C system, International Journal of Refractory Metals & Hard Materials 26 (2008) 372–382.
[25] R.Q. Huang, Z.L. Li, Y.H. Jiang, R. Zhou, F. Gao, Thermal shock cracks initiation and propagation of WCp/steel substrate surface composite at 500°C, Applied Mechanics & Materials 109 (2012) 253–260.
[26] O.O. Eso, F. Peng, Z.Z. Fang, Kinetic model for cobalt gradient formation during liquid phase sintering of functionally graded WC–Co, International Journal of Refractory Metals & Hard Materials 25 (2008) 286–292.
[27] X. Liu, X. Song, J. Zhang, S. Zhao, Temperature distribution and neck formation of WC–Co combined particles during spark plasma sintering, Materials Science & Engineering: A 488 (2008) 1–7.
[28] M. Fitzsimmons, V.K. Sarin, Development of CVD WC–Co coatings, Surface & Coatings Technology 137 (2001) 158–163.
[29] G.B.B. Bolelli, G. Coletta, et al., Wear and corrosion behaviour of HVOF WC—CoCr/CVD DLC hybrid coating systems deposited onto aluminium substrate, Surface & Coatings Technology 205 (2011) 4211–4220.
[30] A. Kurlov, Effect of sintering temperature on the phase composition and microhardness of WC-8 wt% Co cemented carbide, Inorg. Mater. 43 (2007) 602–607.
[31] Y. Miyakoshi, K. Takazawa, K. Tagashira, S. Kamota, H. Takahashi, M. Maruyama, et al., Microstructure and strength of interface in joint of WC-40mass% Co alloy/carbon steel, Journal of the Japan Society of Powder and Powder Metallurgy 44 (1997) 958–962.
[32] A.S. Kurlov, A.A. Rempel', Effect of sintering temperature on the phase composition and microhardness of WC-8 wt % Co cemented carbide, Inorg. Mater. 43 (2007) 602–607.
[33] A. Inoue, T. Masumoto, Carbide reactions (M 3 C → M 7 C 3 → M 23 C 6 → M 6 C) during tempering of rapidly solidified high carbon Cr-W and Cr-Mo steels, Metall. Trans. A. 11 (1980) 739–747.
[34] G.S. Upadhyava, Cemented Tungsten Carbides: Production, and Testing, Noyes Publications, New Jersey, 1998 7–54.
[35] B. Uhrenius, H. Pastor, E. Pauty, On the composition of Fe-Ni-Co-WC-based cemented carbides, Int. J. Refract. Met. Hard Mater. 15 (1997) 139–149.
[36] L. Zhong, X. Zhang, S. Chen, Y. Xu, H. Wu, J. Wang, Fe–W–C thermodynamics and in situ preparation of tungsten carbide-reinforced iron-based surface composites by solid-phase diffusion, Int. J. Refract. Met. Hard Mater. 57 (2016) 42–49.
[37] D.V. Suetin, I.R. Shein, A.L. Ivanovskii, Structural, electronic and magnetic properties of ether carbides (Fe3W3C, Fe6W6C, Co3W3C and Co6W6C) from first principles calculations, Physica B Condensed Matter 404 (2009) 3544–3549.
[38] Z.-H. Xu, X. Li, Influence of equi-biaxial residual stress on unloading behaviour of nanoindentation, Acta Mater. 53 (2005) 1913–1919.
[39] B. Taljat, G.M. Pharr, Measurement of residual stresses by load and depth sensing spherical indentation, MRS Online Proceedings Library Archive 1999, p. 594.
[40] H. Song, H. Yavas, E.V. Giessen, S. Papanikolaou, Discrete dislocation dynamics simulations of nanoindentation with pre-stress: hardness and statistics of abrupt plastic events, Journal of the Mechanics and Physics of Solids 123 (2019) 332–347.
[41] T.Y. Tsui, W. Oliver, G.M. Pharr, Influences of stress on the measurement of mechanical properties using nanoindentation: part I. Experimental studies in an aluminum alloy, J. Mater. Res. 11 (3) (1996) 752–759.
[42] J.G. Swadener, B. Taljat, G.M. Pharr, Measurement of residual stress by load and depth sensing indentation with spherical indenters, J. Mater. Res. 16 (2001) 2091–2102.
[43] A. Bolshakov, W.C. Oliver, G.M. Pharr, Influences of stress on the measurement of mechanical properties using nanoindentation: part II. Finite element simulations, J. Mater. Res. 11 (1996) 760–768.
[44] J. Gibmeier, S. Hartmann, B. Scholtes, Effect of applied and residual stresses on the analysis of mechanical properties by means of instrumented indentation techniques, Mater. Sci. Forum 490–491 (2005) 454–459.
[45] S. Carlsson, P.L. Larsson, On the determination of residual stress and strain fields by sharp indentation testing.: Part I: theoretical and numerical analysis, Acta Mater. 49 (2001) 2193–2203.
[46] C. Xi, Y. Jin, A.M. Karlsson, On the determination of residual stress and mechanical properties by indentation, Materials Science & Engineering A 416 (2006) 139–149.
[47] Suresh S, Giannakopoulos AE. A new method for estimating residual stresses by instrumented sharp indentation. Acta Mater..46:5755–67.
[48] M. Damadam, S. Shao, I. Salehinia, I. Mastorakos, G. Ayoub, H.M. Zbib, Strength and plastic deformation behavior of nanolaminate composites with pre-existing dislocations, Comput. Mater. Sci. 138 (2017) 42–48.
[49] A. Barnoush, Correlation between dislocation density and nanomechanical response during nanoindentation, Acta Mater. 60 (2012) 1268–1277.

[50] A. Barnoush, M.T. Welsch, H. Vehoff, Correlation between dislocation density and pop-in phenomena in aluminum studied by nanoindentation and electron channeling contrast imaging, Scr. Mater. 63 (2010) 465–468.
[51] S. Pugh, XCII. Relations between the elastic moduli and the plastic properties of polycrystalline pure metals, The London, Edinburgh, and Dublin Philosophical Magazine and Journal of Science 45 (1954) 823–843.
[52] K. Persson, Materials Data on WC (SG:221) by Materials Project, 2016.
[53] B. Xiao, J.D. Xing, J. Feng, C.T. Zhou, Y.F. Li, W. Su, et al., A comparative study of Cr7C3, Fe3C and Fe2B in cast iron both from ab initio calculations and experiments, Journal of Physics D Applied Physics 42 (2009), 115415.
[54] Y. Li, Y. Gao, Z. Fan, B. Xiao, Q. Yue, T. Min, et al., First-principles study on the stability and mechanical property of eta M 3 W 3 C (M=Fe, Co, Ni) compounds, Physica B Physics of Condensed Matter 405 (2010) 1011–1017.
[55] K. Persson, Materials Data on Cr23C6 (SG:225) by Materials Project, 2016.
[56] P. Liu, D. Chen, Q. Wang, P. Xu, M. Long, H. Duan, Crystal structure and mechanical properties of nickel–cobalt alloys with different compositions: a first-principles study, J. Phys. Chem. Solids 137 (2020), 109194.
[57] J. Gump, H. Xia, M. Chirita, R. Sooryakumar, M. Tomaz, G. Harp, Elastic constants of face-centered-cubic cobalt, J. Appl. Phys. 86 (1999) 6005–6009.
[58] K. Persson, Materials Data on Co (SG:186) by Materials Project, 2016.
[59] Z. Li, Y. Jiang, R. Zhou, F. Gao, Q. Shan, J. Tan, Thermal fatigue mechanism of WC particles reinforced steel substrate surface composite at different thermal shock temperatures, J. Alloys Compd. 596 (2014) 48–54.
[60] X. Liu, X. Song, H. Wang, X. Liu, F. Tang, L. Hao, Complexions in WC-Co cemented carbides, Acta Mater. 149 (2018).
[61] Z. Li, P. Wang, Q. Shan, Y. Jiang, H. Wei, J. Tan, The particle shape of WC governing the fracture mechanism of particle reinforced iron matrix composites, Materials 11 (2018) 984.